Journal of the Meteorological Society of Japan

EARLY ONLINE RELEASE

The DOI for this manuscript is

DOI:10.2151/jmsj.2024-007

J-STAGE Advance published date: December 27, 2023

Short-Term Predictability of Extreme Rainfall Using Dual-Polarization Radar Measurements

Aina OTSUBO[1)] **and Ahoro ADACHI**[1),2)]

[1)] *Meteorological College, Kashiwa, Chiba, Japan*
[2)] *Meteorological Research Institute, Tsukuba, Ibaraki, Japan*

December 17, 2023

Corresponding author: Aina Otsubo, Japan Meteorological Agency, 3-6-9 Toranomon, Minato-ku, Tokyo 105-8431, Japan.
E-mail: a-otsubo@met.kishou.go.jp

Abstract

Dual-polarization radar often detects columnar regions of enhanced differential reflectivity (Z_{DR}) extending vertically above the environmental 0 °C level. Indicative of supercooled liquid drops and wet ice particles lofted by strong updrafts, these Z_{DR} columns are increasingly understood to be of use in predicting extreme rainfall. With the aim of achieving practical application of Z_{DR} column measurements, this paper focuses on the relationship between the height of Z_{DR} columns and rainfall intensity near the ground.

All the data on Z_{DR} columns analyzed in this study was collected from weather radar stations in Japan. The height of each column and rainfall rates at low levels were analyzed using an automated algorithm. A regression analysis result reveals peak column height to be positively correlated with maximum rainfall rate near ground level, and that rainfall intensity on the ground is likely to exceed 50 $\mathrm{mm\,h^{-1}}$ when radar identifies a Z_{DR} column. Furthermore, extreme rainfall with an intensity of 180 $\mathrm{mm\,h^{-1}}$ or more is likely associated with a column over 3 km tall from the 0 °C level. These findings suggest that surveillance of Z_{DR} columns can contribute to the reliability of very short-range forecasts or nowcasts as well as assist with the issue of early warnings of extreme rainfall and flash floods.

Keywords extreme event; radar; Z_{DR} column; rainfall intensity; short-range forecast

1. Introduction

Increasing global warming has resulted in greater frequency and intensity of extreme precipitation events around the world, caused by increased evaporation and atmospheric water-holding capacity attributed to higher temperatures, as governed by the Clausius–Clapeyron (CC) relation (e.g., Min et al. 2011; Seneviratne et al. 2021). Numerous studies have been carried out on the association between atmospheric temperature and heavy precipitation, some of which demonstrate that the frequency of short-duration extremes may even exceed predictions based on the CC rate (e.g., Lenderink and Van Meijgaard 2008) and that the intensity of sub-daily extremes increases more rapidly than that of daily-scale events (e.g., Westra et al. 2014).

In recent decades, heavy precipitation events have often impacted human society and the environment, mainly through rain-triggered disasters such as floods, the most common natural hazard worldwide. Across the 2001 - 2020 period, an average of 357 annual catastrophic events were recorded, in which floods (163) predominated (Centre for Research on the Epidemiology of Disasters 2022b). In 2022, India and Pakistan experienced devastating floods after extreme rainfall, each with more than one thousand deaths (Centre for Research on the Epidemiology of Disasters 2022a). Flood risks such as these are predicted to increase with the acceleration of urbanization, due to the expansion of impervious surfaces and subsequent loss of infiltration capacity (e.g., Tingsanchali 2012).

The major damage that is often caused by extreme rainfall is prompting research on enhancing the resolution of operational numerical weather prediction models to provide more realistic forecasts of local weather, especially of precipitation. Despite the increasing accuracy of rainfall forecasts, an element of uncertainty remains in all models. A large proportion of this uncertainty derives from assumptions made in the parameterization of unresolved cloud microphysical processes. However, a certain amount of information can be gained from dual-polarization radar observations (e.g., Roberts and Lean 2008; Seifert 2011; Adachi et al. 2015; Trömel et al. 2021).

The National Weather Service (NWS) completed the dual-polarization upgrade of its Weather Service radar (WSR-88D) in 2013 (Gerard 2021), and the Japan Meteorological Agency (JMA) started upgrading its operational weather radar in March 2020 (Japan Meteorological Agency 2022). Sending and receiving signals with both horizontal and vertical polarization, dual-polarization radar, or polarimetric radar can provide beneficial polarimetric variables that deliver information concerning hydrometeor size, shape, and orientation by comparing the amplitudes and phases of the signals returned at both polarizations. Of these variables, the differential reflectivity, or Z_{DR}, is a function of the shapes of hydrometeors. Higher values of Z_{DR} are recorded when raindrops grow and take on a more oblate spheroidal shape.

Polarimetric radar observations of deep convective clouds frequently show upward extensions of positive Z_{DR} above the environmental 0 °C level where ice particles are usually distributed. These signatures, known as Z_{DR} columns, contain supercooled liquid drops lofted by strong updrafts (Kumjian 2013b). Recent studies have shown that Z_{DR} column evolution is linked to convective cloud development. For example, Kumjian et al. (2012) clarified the correlation between Z_{DR} column height and updraft intensity using a simplified theoretical model, and Adachi et al. (2013) presented a method of detecting potentially hazardous convective clouds that produce extreme rainfall by identifying Z_{DR} columns. Picca et al. (2010) and Kumjian et al. (2014) describe how growth in the horizontal and vertical directions of Z_{DR} columns precedes, by 10 - 30 minutes, an increase in low-level radar reflectivity. Snyder et al. (2015) proposed an automated Z_{DR} column algorithm designed to monitor the changes in Z_{DR} column height and provide near-real-time information on the intensity and location of updrafts. Kuster et al. (2020) state that Z_{DR} columns can be used to arrive at specific warning decisions for convective storms.

Despite these findings, the relationship between Z_{DR} column height and rainfall intensity produced by the convective cloud has hitherto not been quantitatively evaluated. This prompted us to investigate the relationship between peak Z_{DR} column height and momentary maximum rainfall rate near ground level using regression analysis of the rapid-update radar data observed in the Tokyo metropolitan area with a view to the more general application of Z_{DR} column information to short-term rainfall prediction.

This paper focuses on isolated Z_{DR} columns producing localized heavy rainfall for ease of analysis and looks at those measured by the dual-polarization Doppler weather radar at Haneda airport (Haneda radar) on 11 July 2021. The next section describes the instrumentation and analytical data. Section 3 covers data analysis techniques using dual-polarization radar measurements. Section 4 provides the analysis results of the relationship between Z_{DR} column height and rainfall intensity near the ground, followed by our Discussion in Section 5. The paper closes with a brief conclusion in Section 6 that summarizes our findings.

2. Instrumentation and analytical data

2.1 Dual-polarization weather radar

Doppler Radar for Airport Weather (DRAW) has been installed at major airports in Japan to monitor weather conditions for the safe operation of aircraft. The data sources in this study are the Haneda radar for the most part, but also the Narita radar at Narita International Airport for 0 °C level estimation. Haneda and Narita airports both operate C-band dual-polarized radar that provides a suite of polarimetric variables including the reflectivity factors ($Z_{\mathrm{H}}, Z_{\mathrm{V}}$), differential reflectivity (Z_{DR}), total differential phase shift (Ψ_{DP}), specific differential phase (K_{DP}), and co-polar correlation coefficient (ρ_{HV}). Their data are collected up to a maximum range of 120 km with an azimuthal resolution of 0.7° and a radial resolution of 150 m. The volume scans are updated every five minutes and each scan comprises twelve plan-position indicator (PPI) scans at elevation angles of 0.7°, 1.1°, 1.5°, 2.1°, 2.8°, 3.8°, 5.1°, 6.9°, 9.2°, 12.5°, 17.0°, and 90°. Five PPI scans at an elevation angle of 0.7° are included in each volume scan to improve the time resolution near the ground. The details of the Haneda radar are given in Table 1.

Table 1

2.2 Surface observations

a. Disdrometer

The Parsivel is a laser-based optical disdrometer for simultaneous measurement of PARticle SIze and VELocity of hydrometeors, designed by Löffler-Mang and Joss (2000) and formerly manufactured by PM Tech, but by OTT after 2004. In this study, we employed an OTT Parsivel (Version 1) disdrometer installed at the Kumagaya observation site.

The Parsivel is equipped with a laser sensor that produces a horizontal sheet of light measuring 30 mm $\times$ 180 mm, with a transmitter and receiver integrated into a single protective housing. Precipitation particles passing through the laser beam block a portion of the beam in proportion to their diameter, causing a reduction of the output voltage. The maximum attenuation of the signal is a measure of the particle size, and the time taken for the particle to pass through the laser beam allows an estimate of its velocity (e.g., Löffler-Mang and Joss 2000; OTT 2005).

The OTT Parsivel disdrometer can estimate particle sizes ranging from 0.2 mm to 25 mm in diameter and velocities from 0.2 $\mathrm{m\,s^{-1}}$ to 20 $\mathrm{m\,s^{-1}}$. After determining their diameters and velocities, it classifies them into one of 32 separate size and velocity classes with a high temporal resolution of one minute. It is therefore more suitable than a tipping bucket rain gauge for observations of heavy convective rainfall events of the type shown in this study (Section 4.1).

b. *Surface observation network*

The Automated Meteorological Data Acquisition System (AMeDAS), an observation network of Automatic Weather Stations (AWSs) run by the JMA, measures precipitation, wind direction and speed, temperature, and humidity to support real-time monitoring of weather conditions. The JMA currently operates about 1,300 rain gauges at average intervals of 17 km nationwide. Each gauge records the amount of precipitation in units of 0.5 mm with a temporal resolution of ten minutes (Japan Meteorological Agency 2021). In this study, precipitation data obtained from the Kumagaya observation site is used for accuracy verification of rainfall rates from the co-located disdrometer.

2.3 Case information

The data analyzed in this study were collected using the abovementioned instruments from 13:00 JST (Japan Standard Time: JST = UTC + 9 h) to 18:00 JST on 11 July 2021. On that day, dozens of Z_{DR} columns were observed by the Haneda radar, and the atmospheric condition was unstable due to a stationary front, resulting in heavy precipitation over the Kanto region (eastern Japan). Figure 1 shows the distribution of the rainfall estimates and the locations of the instruments and the Tateno aerological observation site (Section 3.1).

The findings from the quantitative data analysis are validated using the data collected from 12:00 JST to 16:00 JST on 12 August 2020 (Section 5.5), when atmospheric instability caused by elevated ground temperatures led to convective heavy precipitation over the Kanto region, coupled with high atmospheric pressure across eastern and western regions of Japan. Fig. 1

3. Data analysis techniques

To initiate the analysis, radar data expressed as radar-centered spherical coordinate were converted into geographic form as presented by Karney (2011). Non-meteorological data with correlation coefficients (ρ_{HV}) of below 0.8 and standard deviations of Ψ_{DP} exceeding 4° were removed (e.g., Ryzhkov and Zrnic 1998). Subsequently, the Z_{DR} biases introduced in the radar hardware were corrected through regression analysis between Z_{H} and Z_{V} using radar measurements at vertical incidence in light rain (e.g., Bringi and Chandrasekar 2001). The reduction factors given by Teschl et al. (2008) were employed to calibrate the effect of elevation angles on both Z_{DR} and K_{DP}. Using the elevation-corrected K_{DP}, Z_{H} and Z_{DR} were corrected for their attenuation as described in Bringi and Chandrasekar (2001).

3.1 Z_{DR} column height

Z_{DR} columns are identified as regions of high Z_{DR} extending above the environmental 0 °C level, the height criterion. Since the signature of a melting layer, known as the "bright band," is more evident in ρ_{HV} fields than in Z_H fields (e.g., Kumjian 2013b), vertical distributions of ρ_{HV} were utilized to estimate the 0 °C level in this study. On the basis of the model profile of ρ_{HV} adopted by Brandes and Ikeda (2004), we estimated the 0 °C level at the top of the bright-band signature, assuming the 0 °C level to be constant over the Kanto region while the data were collected. Unlike other analyses, the data here were acquired by the Narita radar around 17:30 JST when the signature appeared most clearly, not by the Haneda radar because the signature was too obscure to estimate the 0 °C level. Figure 2 shows an example of the distribution maps, in which the vertical axis represents the height above ground level (AGL). The estimated 0 °C level approximately corresponds to the results of aerological observations at the Tateno site, located about 60 km northeast of the Haneda radar. Fig. 2

Given that vertical resolutions become coarser with increasing elevation angle, we adopted a fixed 3-dB threshold to define the periphery of the Z_{DR} columns to obtain a more accurate estimation in preference to the 1- or 2-dB threshold often used in other studies (e.g., Kumjian et al. 2014; Snyder et al. 2015). Accordingly, in this study, the Z_{DR} column height is the maximum height of the 3-dB Z_{DR} contour from the 0 °C level. Each column height in the time series was estimated by interpolating data along the movement direction of the center, determined from the PPI scan data, with a width of 1 km (see Fig. 3a for a sample column, called "Column A" hereinafter) and averaging the vertical locations of n points that are selected in descending order from the highest one on the periphery, given that n grid cells exist within 1 km along the horizontal axis. Here, the advective velocity of a cloud is not taken into account because column height is immune to horizontal cloud motion. The central axis of each column was also determined by averaging the horizontal locations of the highest n points on the periphery. Ultimately, the column height and the central axis at the time when column height reached a peak were ascertained, along with the observation time. An example of the estimated height and central axis of Column A is shown in Fig. 3b. Note that the differential reflectivity Z_{DR} is linearly interpolated in the figure. Fig. 3

3.2 Radar rainfall estimation

A wide variety of physical and empirical approaches are generally taken to estimate rainfall rates from polarimetric radar variables. In one of these methods, Cifelli et al. (2011) describe an algorithm called CSU-ICE, which discriminates between pure rain and mixed precipitation using the precipitation ice fraction in a radar volume. The ice fraction is estimated using the difference reflectivity Z_{DP}, defined as

$$Z_{\mathrm{DP}} = 10 \log_{10} \left(Z_{\mathrm{H}} - Z_{\mathrm{V}} \right), \tag{1}$$

where Z_{H} and Z_{V} are linear scale values. However, Z_{DP} may be inaccurate in widespread heavy rain events such as those analyzed in this study due to the attenuation effects of Z_{H} and Z_{V} in the C-band. We therefore applied the CSU-ICE algorithm for mixed precipitation using $R(K_{\mathrm{DP}})$ and $R(Z_{\mathrm{H}})$ to all samples. This algorithm is the same as that which JMA currently employs, expressed as

$$R(K_{\mathrm{DP}}, Z_{\mathrm{H}}) = \begin{cases} R(K_{\mathrm{DP}}) = 129 \left(\frac{K_{\mathrm{DP}}}{f} \right)^{0.85} & \text{if } K_{\mathrm{DP}} > 0.6 \text{ deg/km and } Z_{\mathrm{H}} > 38 \text{ dBZ;} \\ R(Z_{\mathrm{H}}) = \left(0.005 \times 10^{\frac{Z_{\mathrm{H}}}{10}} \right)^{\frac{1}{1.6}} & \text{otherwise,} \end{cases} \tag{2}$$

where R is rainfall rate in $\mathrm{mm\,h^{-1}}$ and f is a radar frequency in GHz (Bringi and Chandrasekar 2001). Note that Z_{H} here is not a rain-only reflectivity but a version observed and corrected.

$R(K_{\mathrm{DP}})$ is commonly exploited because of its high accuracy when used for heavy rainfall estimation, since K_{DP} has the advantage of being immune to attenuation and is less dependent on the variation of drop size distribution (DSD). In contrast, its low accuracy in light rain results from the fact that K_{DP} is not sensitive to spherical particles, and its signal falls below the background noise level (e.g., Sachidananda and Zrnic 1986). Therefore, a traditional $Z-R$ relation, or $R(Z_{\mathrm{H}})$, applies with low K_{DP} and/or reflectivity, mostly in light rain after Z_{H} being corrected. Based on the assumption of Marshall-Palmer DSD (Marshall and Palmer 1948), $R(Z_{\mathrm{H}})$ is strongly affected by variability of precipitation type (e.g., Bennartz and Petty 2001). Taking into account the uncertainties inherent in DSD parameterization, we additionally calibrated Z_{H} by minimizing discrepancies in rainfall rates between Z_{H}-derived estimates and the disdrometer measurements described in the Appendix.

3.3 Low-level maximum rainfall rate

The maximum rainfall rate near ground level associated with each column was estimated from the data observed at the lowest elevation angle of 0.7° by the Haneda radar. Although radar data at this angle are subject to beam blockage due to ground clutter in certain directions, as shown in Fig. 4, the highest temporal resolution of one minute is necessary for analyzing the time series of convective rainfall. Each maximum rainfall rate in the time series was estimated by

1. extracting rainfall rates in a rectangular area measuring 10 km × 30 km between 5 km to windward and 25 km to leeward from the central axis at the time when column height reached a peak, based on wind speed and direction, as shown in Fig. 4, and

2. averaging the highest 5% of the extracted rainfall rates.

Ultimately, the estimated maximum rainfall rates were searched for the highest one, or momentary maximum rainfall rate, within 5 - 30 minutes after the observation of peak column height (Section 3.1), whose time range is based on lag correlations shown by Picca et al. (2010) and Kumjian et al. (2014). The lag time between observations of peak column height and momentary maximum rainfall rate near the ground was also calculated, as depicted in Fig. 5.

Fig. 4

Fig. 5

4. Relationship between peak Z_{DR} column height and maximum rainfall rate

Recent studies have demonstrated Z_{DR} column height to be closely associated with updraft intensity; it increases before producing high reflectivity at low levels (e.g., Kumjian et al. 2014, among others). To what extent, therefore, is it correlated with the intensity of rainfall at ground level? To address this remaining question, we explored the correlation between peak Z_{DR} column height and momentary maximum rainfall rate near ground level using the data acquired by dual-polarization radar.

On 11 July 2021, the Haneda radar observed tens of Z_{DR} columns as columnar regions of enhanced Z_{DR} extending vertically above the estimated

0 °C level of 4.6 km AGL. Thirteen of these were selected as sample columns in this study because they remained at sufficient distances from each other to permit quantitative analysis. For each column, the maximum height in the time evolution, or peak column height, was automatically calculated, as described in Section 3.1. The maximum rainfall rate associated with each column was then estimated using the current JMA algorithm of $R(K_{\rm DP}, Z_{\rm H})$, as detailed in Sections 3.2 and 3.3. Before conducting a regression analysis between the peak column height and the maximum rainfall rate, we validated the radar rainfall estimates at the lowest elevation angle of 0.7° by comparison with disdrometer measurements on the ground as follows.

4.1 Validation of rainfall estimates

Figure 6 displays the rainfall estimates from the Haneda radar compared with those from the disdrometer installed at the Kumagaya observation site. Here, the radar-derived rainfall rates are averaged within 1 - 2 km west of the Kumagaya site on the basis of the environmental wind speed and direction. Given that it takes a few minutes for raindrops to reach ground level, the observation time of the disdrometer is adjusted by three minutes to be equivalent to that of the radar. Although a few outliers are evident, it can be seen in the figure that the radar-derived rainfall estimates agree with the disdrometer measurements with a mean error of 15%. Fig. 6

Fig. 7

Furthermore, we validated rainfall rates derived from the disdrometer by comparison with rain gauge data, both taken from the Kumagaya observation site. Figure 7 shows that the 10-min averaged rainfall rates calculated from the 1-min averaged disdrometer data agree quite well with those from the rain gauge. Taken together with the comparison results shown in Fig. 6, this indicates that the rainfall rates derived from the radar data with a temporal resolution of one minute agree with those observed on the ground.

4.2 Regression analysis

After the validation of radar rainfall estimates, we examined the correlation between the peak Z_{DR} column height and the maximum rainfall rate near ground level. The resultant correlations between the two are plotted in Fig. 8, in which the horizontal and vertical axes respectively represent the height above the 0 °C level and the maximum rainfall rate observed at the lowest elevation angle of 0.7°. Fig. 8

According to the regression analysis results, the regression line is represented as

$$y = 29.0x + 60.2, \tag{3}$$

where x is peak column height (km) and y is maximum rainfall rate ($\mathrm{mm\,h^{-1}}$) near ground level. Although the correlation coefficient is not very high, at 0.64, this result indicates that a taller Z_{DR} column is likely linked to greater production of rainfall. The figure also depicts lag times between observations of peak column height and maximum rainfall rate. About 60% of the lag times for the thirteen columns were recorded within 8 - 12 minutes.

In Fig. 8, Column A has a relatively small residual in the linear regression and a normal lag time of 11.5 minutes among them. By contrast, a data point in another sample column, called "Column B" hereinafter, deviates considerably from the regression line, with the longest lag time of 24 minutes. In the following section, we discuss the evolution of both columns, observed within the rectangular areas in Fig. 9, and the cause of the above deviation.

Fig. 9

5. Discussion

5.1 Evolution of Z_{DR} columns

Recent studies have shown that a tall Z_{DR} column appears when a sufficiently strong updraft lofts large raindrops well above the 0 °C level during the development of convective clouds, and that as the column decays after reaching a peak height, an area of high rainfall rates aloft descends to the ground (e.g., Kumjian et al. 2014). Figures 10 and 11 both depict the time evolution of Column A, beginning with the observation time of the peak column height and ending with that of the maximum rainfall rate. The

3-dB Z_{DR} contour is superimposed over the field of Z_{H}, Z_{DR}, K_{DP}, and ρ_{HV} in Fig. 10, and over that of the highest rainfall rates within a 1km-wide range of the analyzed area in Fig. 11. The observation time at an elevation angle of 3.8° is shown in the upper left corner of each figure. Note that the cross-sections are reconstructed from several elevation-angle scans, thereby involving some degree of interpolation. In Fig. 10, the areas of high Z_{H}, Z_{DR}, and K_{DP} with low ρ_{HV} at heights above the 0 °C level suggest the presence of large raindrops lofted by strong updrafts. In Figs. 11a-c, the areas of maximum rainfall rates gradually descend to the ground as the column decays. Figure 12 shows that the momentary maximum rainfall rate was observed 12 minutes after the column height reached a peak, at 15:14 JST, using the data at the lowest elevation angle of 0.7°. Note that the time is about two minutes later than that shown in Fig. 11c because of the difference in the angles.

Fig. 10

Fig. 11

Fig. 12

Fig. 13

5.2 Interference from hail

Figure 13 depicts the time evolution of Column B, which has different characteristics from other columns (Fig. 8) and considerably high rainfall rates above the 0 °C level, especially at 15:22 JST (Fig. 13c). The presence of hail is expected at these levels at sub-zero temperatures, which is not taken into account in the rainfall estimation algorithm (Section 3.2). For this reason, the rainfall rates estimated for Column B are likely to be inaccurate. To confirm this inference, we examined the vertical distributions of K_{DP}, ρ_{HV}, and $R(K_{\mathrm{DP}}, Z_{\mathrm{H}})$ as in Fig. 14, modified from Fig. 13c. The areas of high K_{DP} overlap only slightly with those of $R(K_{\mathrm{DP}}, Z_{\mathrm{H}}) \geq 150\ \mathrm{mm\,h^{-1}}$, denoted by the dashed contour, which reveals that the estimates of high rainfall rates are in error due to $R(Z_{\mathrm{H}})$ being included in the measurement, caused by low K_{DP} and high Z_{H}. In other words, the mismatch of high K_{DP} and high $R(K_{\mathrm{DP}}, Z_{\mathrm{H}})$ implies incorrect radar rainfall estimation. Moreover, the areas of low ρ_{HV} superimposed with bold contours nearly overlap those of high $R(K_{\mathrm{DP}}, Z_{\mathrm{H}})$, which indicates that hail is present in those areas, since ρ_{HV} decreases in hail-mixed precipitation (Kumjian 2013a). The presence of hail is, therefore, likely to have caused the estimation error by increasing Z_{H} but leaving K_{DP} unaffected. Fig. 14

5.3 Improvement of rainfall estimation

To reduce the effect of interference from hail, we recalculated low-level maximum rainfall rates after eliminating data with $R(K_{\mathrm{DP}}, Z_{\mathrm{H}}) > 1.5R(K_{\mathrm{DP}})$ and $R(K_{\mathrm{DP}}, Z_{\mathrm{H}}) > 100\,\mathrm{mm\,h^{-1}}$ to detect heavy precipitation estimates that are strongly affected by the presence of hail. The recalculation led to an approximately 50% change in Column B but less than 15% for the other columns in the resultant maximum rainfall rates. Note that this algorithm is applicable only to hail-mixed heavy rainfall estimation and does not work for pure rain. The regression equation and the correlation coefficient between rainfall estimates from radar and disdrometer are

$$y = 1.14x + 0.95 \quad (R = 0.85), \tag{4}$$

where x is the rainfall rate derived from disdrometer ($\mathrm{mm\,h^{-1}}$) and y is that from radar ($\mathrm{mm\,h^{-1}}$). They are approximately equal to those shown in Fig. 6b, which supports the validity of the algorithm.

Figure 15 shows the correlations between the peak Z_{DR} column height and the maximum rainfall rate near ground level, where the recalculated results for Columns A and B are denoted as Columns A′ and B′, respectively. The equation of the regression line alters from Eq. (3) to

$$y = 20.7x + 75.6, \tag{5}$$

and the correlation coefficient changes to 0.61 because of the great reduction in the covariance between Z_{DR} column height and low-level maximum rainfall rate. Fig. 15

5.4 Forecast lead time

We explored lag times between observations of the peak column height and the maximum rainfall rate as a function of peak column height, as plotted in Fig. 16, where no correlation is shown, although enhanced Z_{DR}

suggests the presence of large raindrops. Instead, most of the lag times were 9 - 12 minutes regardless of height, and the mean (standard error) was 11.1 ($\pm$ 1.06) minutes. Assuming that it takes several minutes for raindrops to fall from the level of the lowest elevation measurement with the radar to ground level, the expected forecast lead time is about 13 - 15 minutes, which precisely matches the peak lag correlation time arrived at by numerical simulation in Kumjian et al. (2014). The figure also suggests that convective clouds with Z_{DR} columns over 3 km tall have the potential to produce extreme rainfall with an intensity of over 180 $\mathrm{mm\,h^{-1}}$ at ground level. Fig. 16

5.5 Applicability of the quantitative relationship to other cases

To validate the findings from the quantitative analysis on the thirteen columns, we looked at nine Z_{DR} columns observed by the Haneda radar above the estimated 0 °C level of 5.9 km AGL on 12 August 2020, about 1 km higher than that on 11 July 2021. In Fig. 17, the peak column height is positively correlated with the maximum rainfall rate near ground level, and the correlation coefficient is 0.62. Fig. 17

Figure 18 shows the correlation between the two, calculated using both data collected on 11 July 2021 and 12 August 2020. The equation of the regression line is

$$y = 26.3x + 51.8, \quad (6)$$

where x is peak column height (km) and y is maximum rainfall rate ($\mathrm{mm\,h^{-1}}$) near ground level. The correlation coefficient is 0.68, the highest value in this study. These results suggest that the quantitative relationship obtained in this study is applicable to other rainfall events and that rainfall intensity is likely to exceed 50 $\mathrm{mm\,h^{-1}}$ when radar identifies a Z_{DR} column over the Kanto region in summer. Fig. 18

The correlation between the peak column height and the lag time, calculated using the data collected on 12 August 2020, is shown in Fig. 19, in which those on 11 July 2021 are not plotted because of the difference in the estimated 0 °C levels. According to the regression analysis results, the regression line is represented as

$$y = 6.93x - 0.74, \quad (7)$$

where x is peak column height (km) and y is lag time (min). The figure shows a positive correlation with a coefficient of 0.68, which is likely associated with the correlation between Z_{DR} column height and updraft intensity. However, no correlation is shown in Fig. 16. Further analysis of cases in various atmospheric conditions is needed to arrive at a definitive understanding of the difference in correlations between them. Fig. 19

6. Conclusions

The increasing use of dual-polarization radar in recent decades has allowed progressive elucidation of the characteristics of Z_{DR} columns. For example, growth in the volume of a Z_{DR} column appears before an increase in radar reflectivity at low levels (e.g., Picca et al. 2010). The location and height of a Z_{DR} column are closely related to the position and intensity of updrafts, respectively (e.g., Snyder et al. 2015). Although Z_{DR} columns are increasingly regarded as a predictive tool for extreme rainfall, it remains unclear how well they are associated with rainfall intensity on the ground and to what extent they can be applied to weather prediction.

Our quantitative research using dual-polarization radar measurements reveals a positive correlation between peak Z_{DR} column height and maximum rainfall rate near ground level, indicating that Z_{DR} columns should be able to provide useful information on expected rainfall intensity. For instance, when radar identifies a Z_{DR} column, rainfall intensity on the ground is likely to exceed 50 $\mathrm{mm\,h^{-1}}$ and continue to increase while the column grows in height. A column over 3 km tall from the environmental 0 °C level can be a precursor of extreme rainfall with an intensity of 180 $\mathrm{mm\,h^{-1}}$ or more. The heaviest rainfall is likely to occur about 10 - 20 minutes after a Z_{DR} column matures, though more studies are required to determine the definitive forecast lead time. Our findings suggest that Z_{DR} column measurement can help to improve very short-range forecasts and/or nowcasts and lead to early warnings and better disaster management of localized rainfall extremes and the damaging floods that result from them.

On the other hand, the resultant correlation might be improved by applying additional meteorological data or environmental factors. As an example, certain convective parameters, such as convective available potential energy (CAPE), may strengthen the correlation if integrated into the data analysis. Additionally, with further studies on Z_{DR} columns, a better understanding of cloud microphysical processes in convective clouds might, for instance, contribute to the development of numerical weather prediction models through the identification of updraft regions. In brief, more advanced research is needed in future to enhance the effectiveness of operational applications of Z_{DR} columns for severe weather prediction.

Appendix

Disdrometer measurements

The Parsivel disdrometer records rainfall rates derived from its onboard ASDO software, but they tend to be overestimated during heavy rainfall events (Thurai et al. 2011). Adachi et al. (2013) suggest that this tendency is likely to occur because the diameters determined by Parsivel[1] are not volume-equivalent: they are only the maximum horizontal diameters of particles. For this reason, we recalculated rainfall rates using DSD data obtained through converting horizontal diameters of raindrops into volume-equivalent versions on the basis of the model axis ratio presented by Beard and Chuang (1987) and reducing the influence of strong wind and turbulence as proposed by Friedrich et al. (2013). The equation for calculating rainfall rates is expressed as

$$R = 6 \times 10^{-4}\pi \sum_{p=1}^{32} \frac{C_p D_p^3}{S \cdot \Delta t}, \tag{8}$$

where R is rainfall rate ($\mathrm{mm\,h^{-1}}$), C_p and D_p are the number and the volume equivalent diameter (mm) of the particles in the 32 size classes, S is the measuring area ($\mathrm{m^2}$), and Δt is the sampling time (s).

Data Availability Statement

The observational data from radar and disdrometer measurements analyzed in this study, which respectively belong to the Japan Meteorological Agency (JMA) and Meteorological Research Institute (MRI), are available from the corresponding author upon reasonable request. The precipitation data from the rain gauge is available at `https://www.data.jma.go.jp/gmd/risk/obsdl/index.php` (in Japanese).

Acknowledgements

The authors would like to thank Professors Michiko Otsuka, Tomoyuki Kamakura, and Takahiro Ito at Meteorological College for their support and assistance. We are grateful for the constructive comments from Drs. Teruyuki Kato, Hiroshi Yamauchi, Akihito Umehara, and Takashi Unuma of MRI. Drs. Nobuhiro Nagumo, Yusuke Kajiwara, Akira Ooshima, Shuichi Tanaka, and Sohei Yoneda of the JMA's Atmosphere and Ocean Department and others also helped us to improve the quality of this work. Data from the Haneda and Narita radar stations are courtesy of the JMA and were analyzed using *Draft* (Tanaka and Suzuki 2000). Lastly, the first author thanks an English checker, Mr. Eric Sheldon, and her mother, Mrs. Miwako Otsubo, for their heartfelt support.

This work was supported in part by JSPS KAKENHI, Grant Number JP20K04092, and by the Workshops and Symposia (2022K-03), a collaborative research of the Disaster Prevention Research Institute, Kyoto University. The manuscript was greatly improved thanks to two anonymous reviewers.

References

Adachi, A., T. Kobayashi, and H. Yamauchi, 2015: Estimation of raindrop size distribution and rainfall rate from polarimetric radar measurements at attenuating frequency based on the self-consistency principle. *Journal of the Meteorological Society of Japan. Ser. II*, **93(3)**, 359–388.

Adachi, A., T. Kobayashi, H. Yamauchi, and S. Onogi, 2013: Detection of potentially hazardous convective clouds with a dual-polarized C-band radar. *Atmos. Meas. Tech.*, **6(10)**, 2741–2760.

Beard, K. V., and C. Chuang, 1987: A new model for the equilibrium shape of raindrops. *J. Atmos. Sci.*, **44(11)**, 1509–1524.

Bennartz, R., and G. W. Petty, 2001: The sensitivity of microwave remote sensing observations of precipitation to ice particle size distributions. *J. Appl. Meteor.*, **40(3)**, 345–364.

Brandes, E. A., and K. Ikeda, 2004: Freezing-level estimation with polarimetric radar. *J. Appl. Meteor. Climatol.*, **43(11)**, 1541–1553.

Bringi, V. N., and V. Chandrasekar, 2001: *Polarimetric Doppler weather radar: principles and applications.* Cambridge university press, 335–539.

Centre for Research on the Epidemiology of Disasters, 2022a: CRED Crunch

68 - Natural Hazards & Disasters : An overview of the first half of 2022.

Centre for Research on the Epidemiology of Disasters, 2022b: Disasters in numbers 2021.

Cifelli, R., V. Chandrasekar, S. Lim, P. C. Kennedy, Y. Wang, and S. A. Rutledge, 2011: A new dual-polarization radar rainfall algorithm: Application in Colorado precipitation events. *J. Atmos. Oceanic Technol.*, **28(3)**, 352–364.

Friedrich, K., S. Higgins, F. J. Masters, and C. R. Lopez, 2013: Articulating and stationary PARSIVEL disdrometer measurements in conditions with strong winds and heavy rainfall. *J. Atmos. Oceanic Technol.*, **30(9)**, 2063–2080.

Gerard, A., 2021: Research-to-operations/applications success stories. `https://www.nssl.noaa.gov/about/events/review2021/presentations/NSSL2021LabReviewR2XSuccessStories.pdf` (Accessed on 16 Feb 2023).

Japan Meteorological Agency, 2021: Amedas. `https://www.jma.go.jp/jma/en/Activities/amedas/amedas.html` (Accessed on 28 Dec 2022).

Japan Meteorological Agency, 2022: Weather Radar. `https://www.jma.go.jp/jma/en/Activities/radar/radar.html` (Accessed on 16 Feb 2023).

Karney, C. F., 2011: Geodesics on an ellipsoid of revolution. *arXiv preprint arXiv:1102.1215*.

Kumjian, M. R., 2013a: Principles and applications of dual-polarization weather radar. Part I: Description of the polarimetric radar variables. *J. Oper. Meteor.*, **1(19)**, 226–242.

Kumjian, M. R., 2013b: Principles and applications of dual-polarization weather radar. Part II: Warm- and cold-season applications. *J. Oper. Meteor.*, **1(20)**, 243–264.

Kumjian, M. R., S. M. Ganson, and A. V. Ryzhkov, 2012: Freezing of raindrops in deep convective updrafts: A microphysical and polarimetric model. *J. Atmos. Sci.*, **69(12)**, 3471–3490.

Kumjian, M. R., A. P. Khain, N. Benmoshe, E. Ilotoviz, A. V. Ryzhkov, and V. T. Phillips, 2014: The anatomy and physics of Z_{DR} columns: Investigating a polarimetric radar signature with a spectral bin microphysical model. *J. Appl. Meteor. Climatol.*, **53(7)**, 1820–1843.

Kuster, C. M., T. J. Schuur, T. T. Lindley, and J. C. Snyder, 2020: Using

Z_{DR} columns in forecaster conceptual models and warning decision-making. *Wea. Forecasting*, **35(6)**, 2507–2522.

Lenderink, G., and E. Van Meijgaard, 2008: Increase in hourly precipitation extremes beyond expectations from temperature changes. *Nat. Geosci.*, **1(8)**, 511–514.

Löffler-Mang, M., and J. Joss, 2000: An optical disdrometer for measuring size and velocity of hydrometeors. *J. Atmos. Oceanic Technol.*, **17(2)**, 130–139.

Marshall, J. S., and W. M. K. Palmer, 1948: The distribution of raindrops with size. *J. Meteor.*, **5**, 165–166.

Min, S.-K., X. Zhang, F. W. Zwiers, and G. C. Hegerl, 2011: Human contribution to more-intense precipitation extremes. *Nature*, **470(7334)**, 378–381.

OTT, 2005: Operating instructions: Present weather sensor parsivel.

Picca, J. C., M. Kumjian, and A. Ryzhkov, 2010: Z_{DR} columns as a predictive tool for hail growth and storm evolution. *25th Conf. on Severe Local Storms.*

Roberts, N. M., and H. W. Lean, 2008: Scale-selective verification of rainfall accumulations from high-resolution forecasts of convective events. *Mon. Wea. Rev.*, **136(1)**, 78–97.

Ryzhkov, A. V., and D. S. Zrnic, 1998: Polarimetric rainfall estimation in the presence of anomalous propagation. *J. Atmos. Oceanic Technol.*, **15(6)**, 1320–1330.

Sachidananda, M., and D. Zrnic, 1986: Differential propagation phase shift and rainfall rate estimation. *Radio Sci.*, **21(2)**, 235–247.

Seifert, A., 2011: Uncertainty and complexity in cloud microphysics. *Proc. ECMWF Workshop on Model Uncertainty.*

Seneviratne, S., X. Zhang, M. Adnan, W. Badi, C. Dereczynski, A. Di Luca, S. Ghosh, I. Iskandar, J. Kossin, S. Lewis, F. Otto, I. Pinto, M. Satoh, S. Vicente-Serrano, M. Wehner, and B. Zhou, 2021: Weather and climate extreme events in a changing climate. *Climate Change 2021: The Physical Science Basis. Contribution of Working Group I to the Sixth Assessment Report of the Intergovernmental Panel on Climate Change* 1513–1766.

Snyder, J. C., A. V. Ryzhkov, M. R. Kumjian, A. P. Khain, and J. Picca, 2015: A Z_{DR} column detection algorithm to examine convective storm updrafts. *Wea. Forecasting*, **30(6)**, 1819–1844.

Tanaka, Y., and O. Suzuki, 2000: Development of radar analysis software *Draft*. *Preprints of the Spring Conference of Meteor. Soc. Japan*, **77**, 303 (in Japanese).

Teschl, F., W. Randeu, M. Schönhuber, and R. Teschl, 2008: Simulation of polarimetric radar variables in rain at S-, C-and X-band wavelengths. *Adv. Geosci.*, **16**, 27–32.

Thurai, M., W. Petersen, A. Tokay, C. Schultz, and P. Gatlin, 2011: Drop size distribution comparisons between Parsivel and 2-D video disdrometers. *Adv. Geosci.*, **30**, 3–9.

Tingsanchali, T., 2012: Urban flood disaster management. *Procedia engineering*, **32**, 25–37.

Trömel, S., C. Simmer, U. Blahak, A. Blanke, S. Doktorowski, F. Ewald, M. Frech, M. Gergely, M. Hagen, T. Janjic, and others, 2021: Overview: Fusion of radar polarimetry and numerical atmospheric modelling towards an improved understanding of cloud and precipitation processes. *Atmos. Chem. Phys.*, **21(23)**, 17291–17314.

Westra, S., H. J. Fowler, J. P. Evans, L. V. Alexander, P. Berg, F. Johnson, E. J. Kendon, G. Lenderink, and N. Roberts, 2014: Future changes to the intensity and frequency of short-duration extreme rainfall. *Rev. Geophys.*, **52(3)**, 522–555.

List of Figures

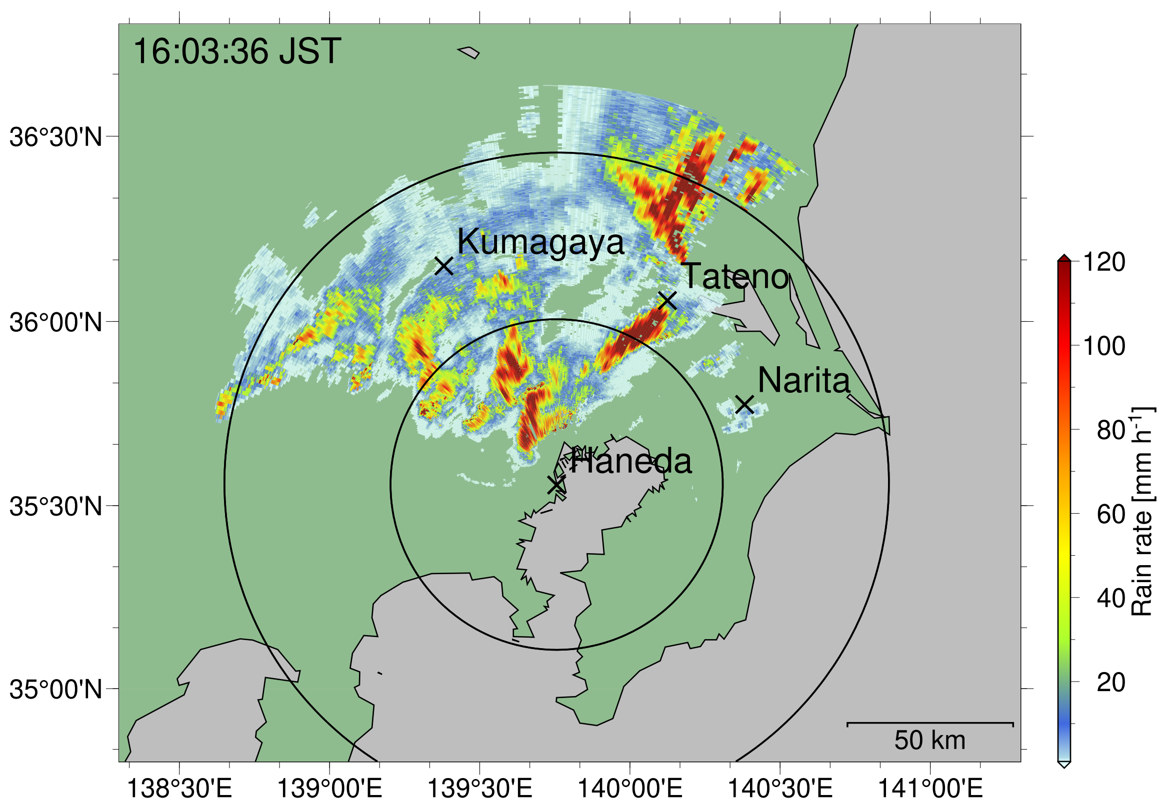

Fig. 1: A snapshot of the estimated rain field from a PPI scan at 1.1° elevation angle performed by the Haneda radar at 16:03 JST on 11 July 2021. Black crosses denote the locations of the Haneda and Narita radar, and the Kumagaya and Tateno observation sites. The two black circles indicate 50-km and 100-km distances from the Haneda radar.

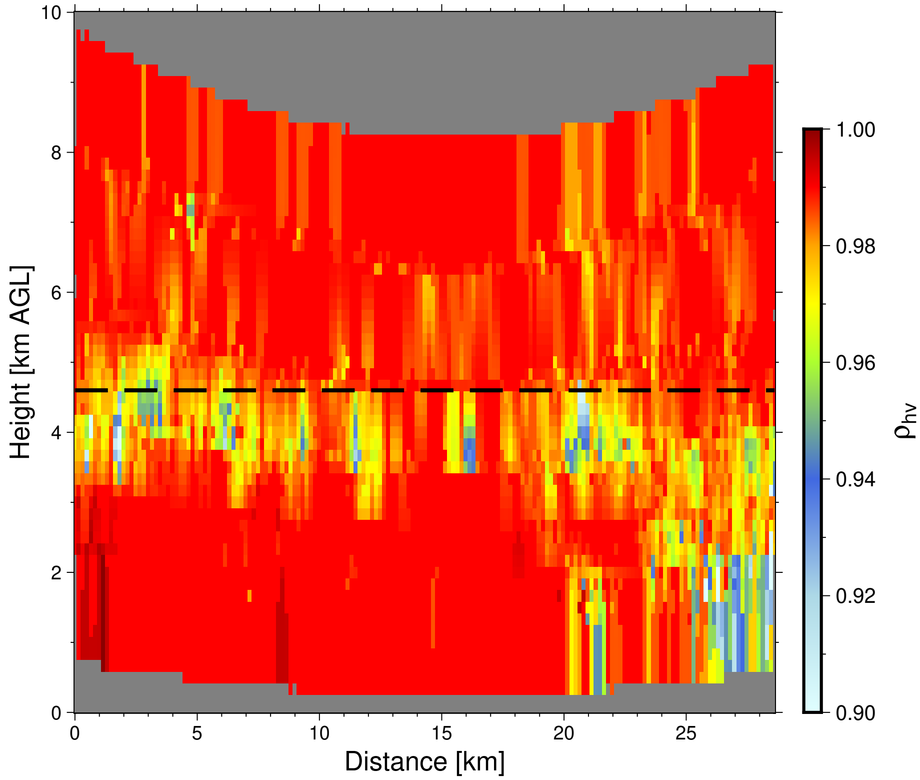

Fig. 2: Vertical distribution of ρ_{HV} composed of PPI scan data at elevation angles between 5.1° and 17.0°, observed by the Narita radar at 17:30 JST on 11 July 2021. The dashed line indicates the estimated 0 °C level of 4.6 km AGL.

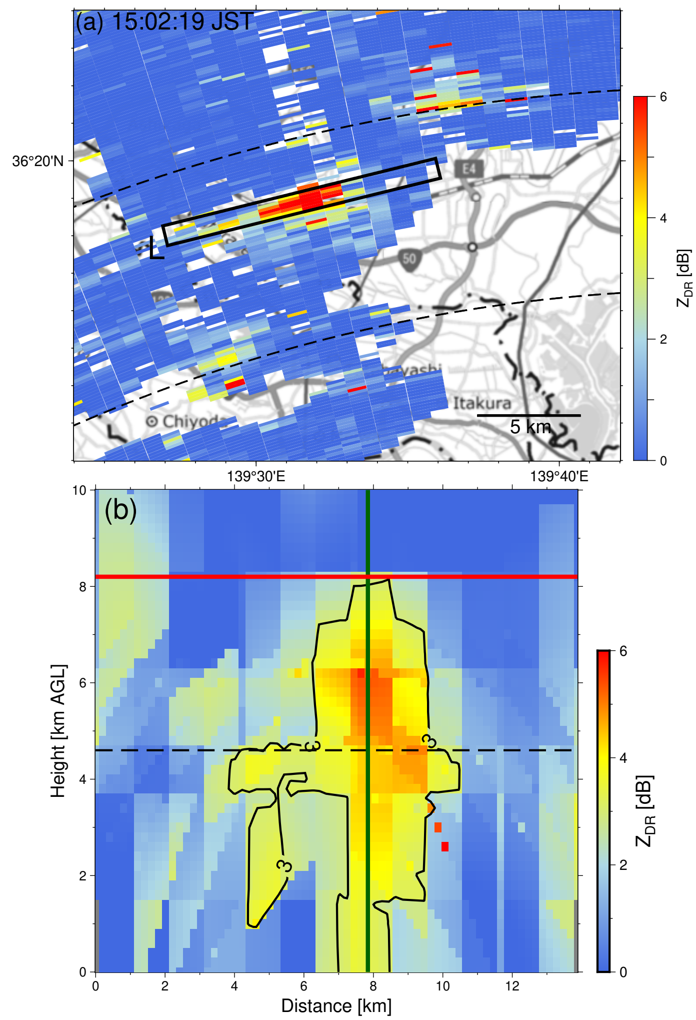

Fig. 3: Snapshots of a sample column

(a) PPI scan of Z_{DR} at 3.8° elevation angle (∼5.8 km AGL) performed by the Haneda radar at 15:02 JST on 11 July 2021. Dashed arcs indicate 80-km and 90-km distances from the radar. The black rectangle (1×14 km) represents the area analyzed within Column A. The base map was obtained from the Geospatial Information Authority of Japan (GSI).

(b) Vertical distribution of Z_{DR} overlaid with lines indicating estimated height (red), central axis (green), estimated 0 °C level of 4.6 km AGL (dashed black), and 3-dB Z_{DR} contour (solid black). The horizontal axis represents the distance from the west end of the rectangle, denoted by letter "L" in (a).

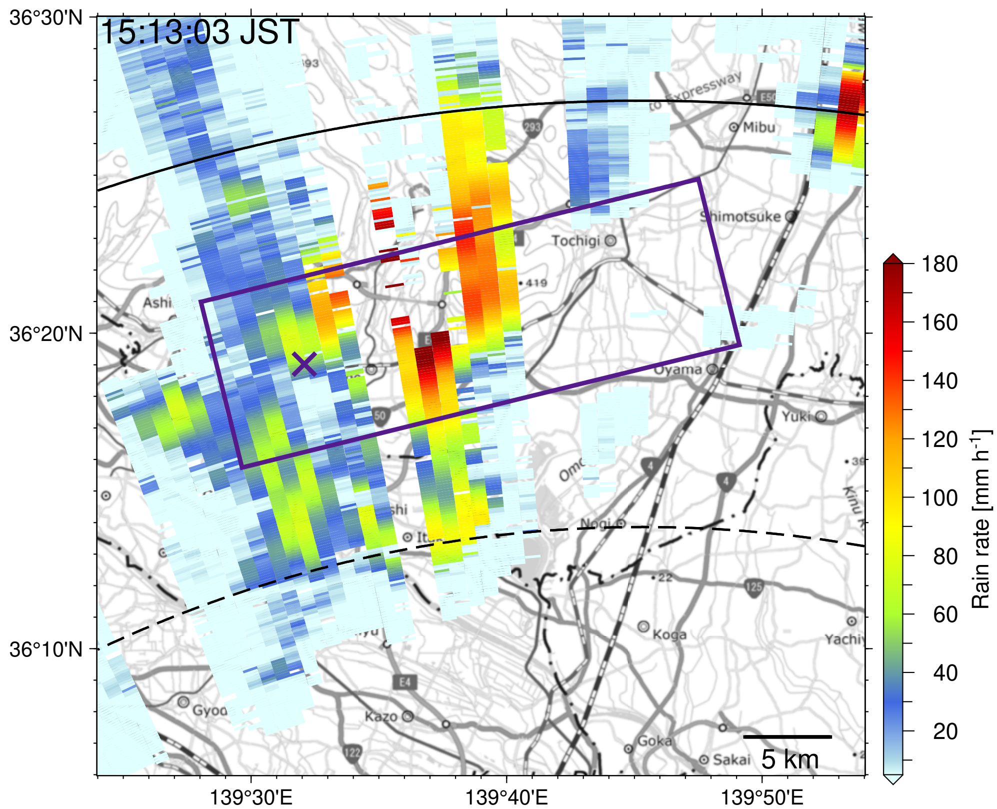

Fig. 4: A snapshot of the estimated rain field from a PPI scan at 0.7° elevation angle performed by the Haneda radar at 15:13 JST on 11 July 2021. The purple cross and rectangle respectively denote the center of Column A and the area (10×30 km) used for the estimation of the maximum rainfall rate near ground level. The black arcs indicate distances of 75 km (dashed) and 100 km (solid) from the Haneda radar. The base map was obtained from the GSI.

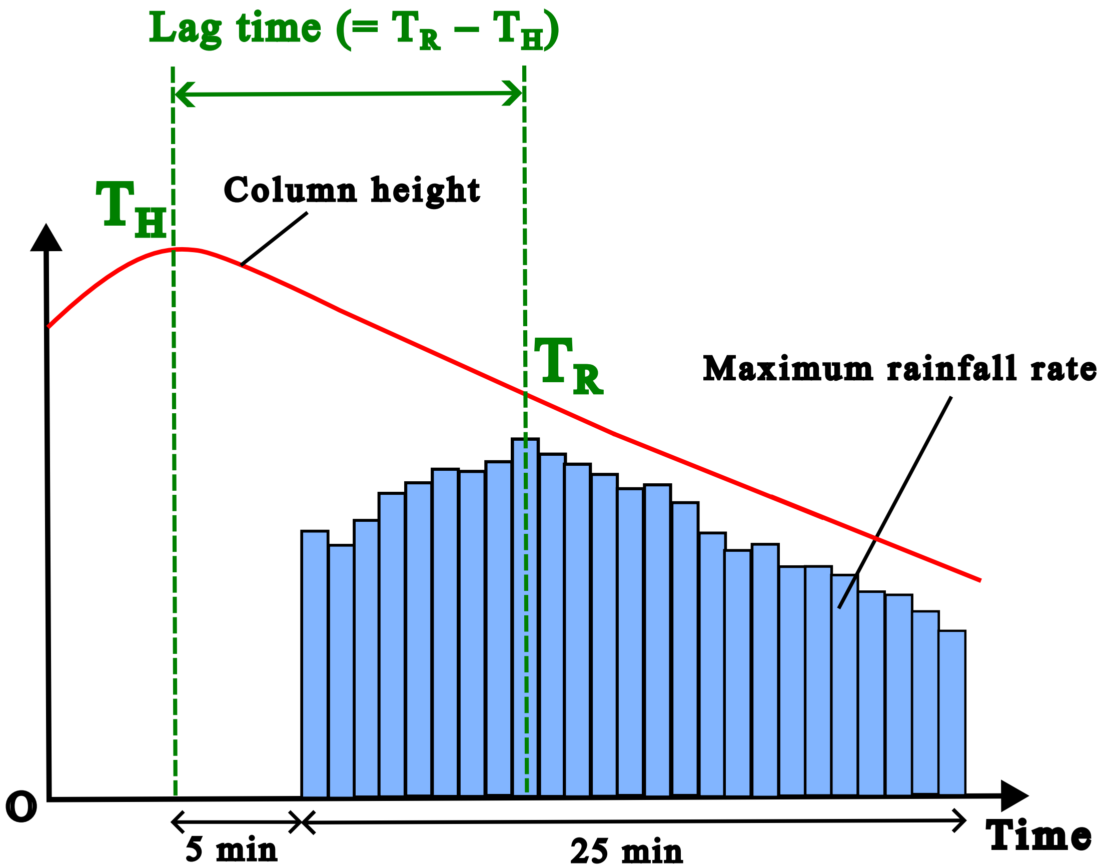

Fig. 5: Schematic diagram showing the lag time calculated by subtracting the observation time of peak column height (T_H) from that of momentary maximum rainfall rate (T_R). The red line and blue bars respectively represent time series of column height and maximum rainfall rate near ground level in the extracted area.

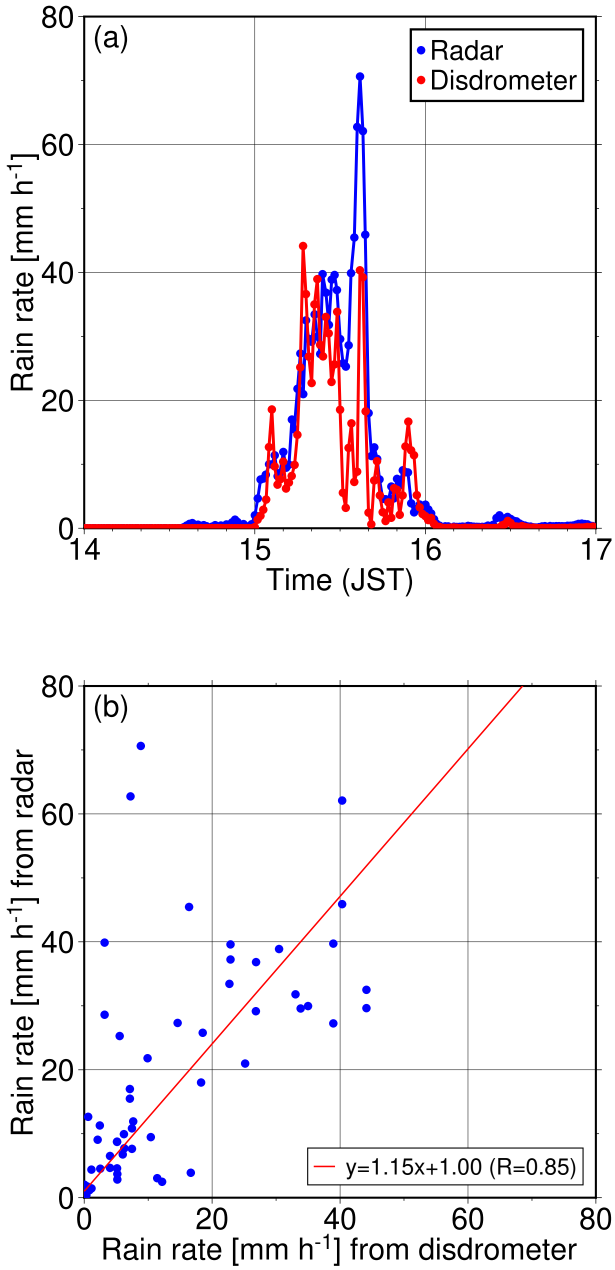

Fig. 6: (a) Time series of rainfall rates from the Haneda radar (blue) and the disdrometer at the Kumagaya site (red); and (b) scatter plots of rainfall rates with a regression line (red), observed on 11 July 2021. The regression equation and the correlation coefficient are shown in the lower right corner.

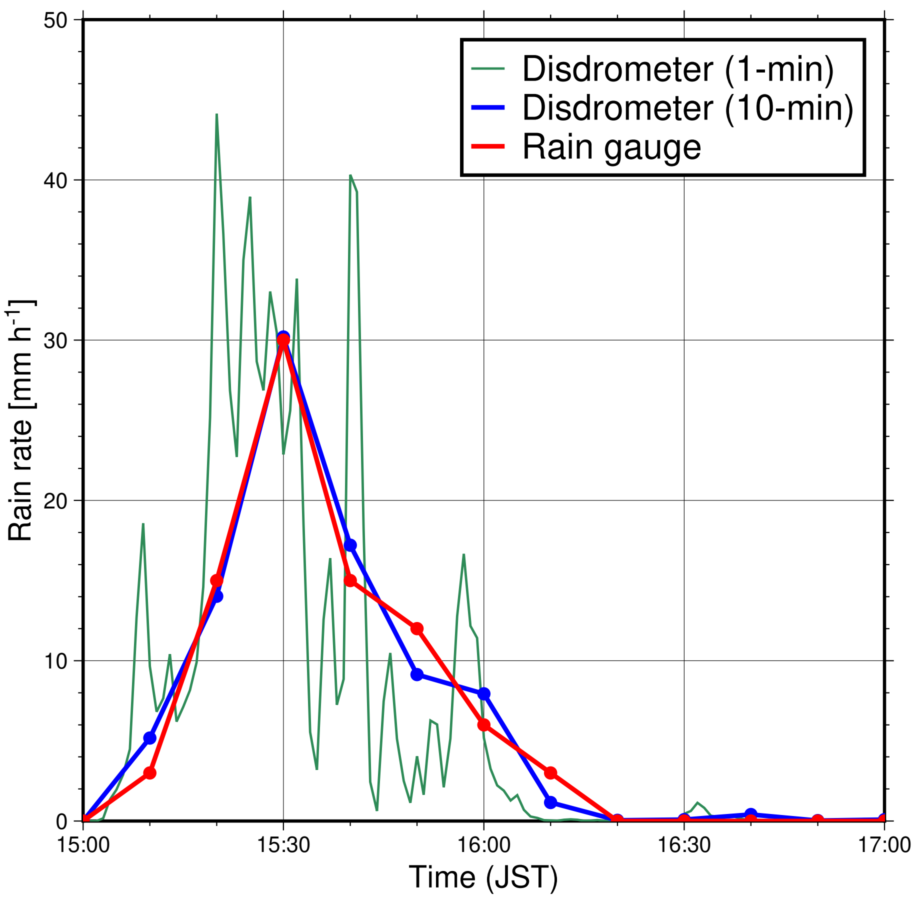

Fig. 7: Time series of rainfall rates from the disdrometer (1-min average in green, 10-min average in blue) and the rain gauge (red) at the Kumagaya site, observed on 11 July 2021.

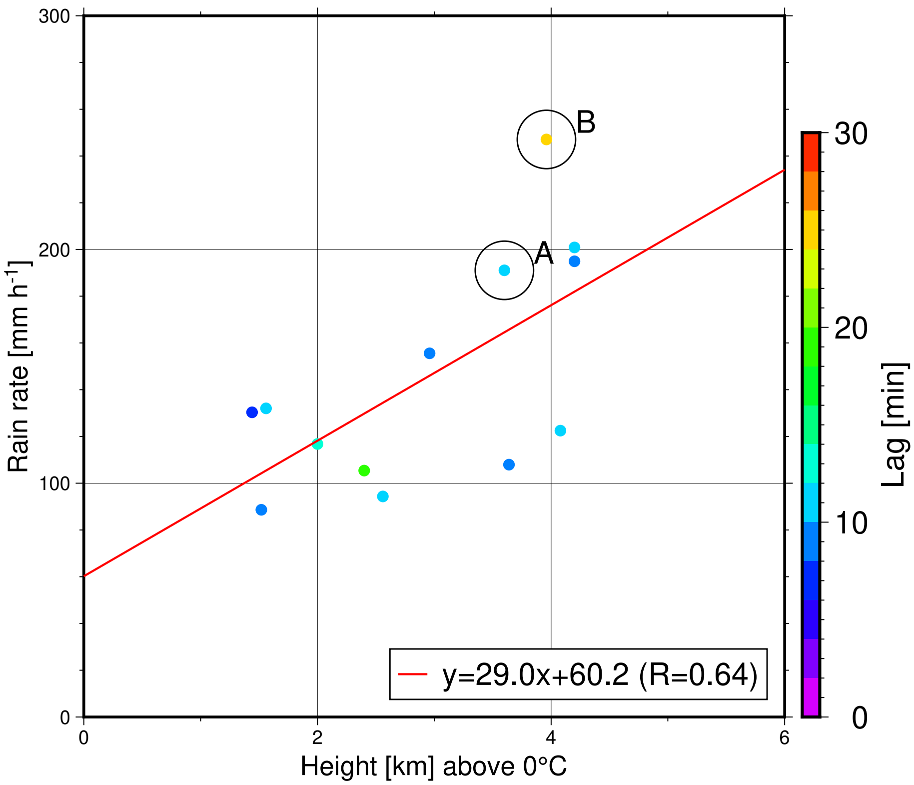

Fig. 8: Scatter plots of peak Z_{DR} column height above the 0 °C level vs. the maximum rainfall rate at low levels, observed on 11 July 2021, with the color scale representing the lag time between observations. Black circles denote the data for Columns A and B, and the red line shows the linear regression. The regression equation and the correlation coefficient are shown in the lower right corner.

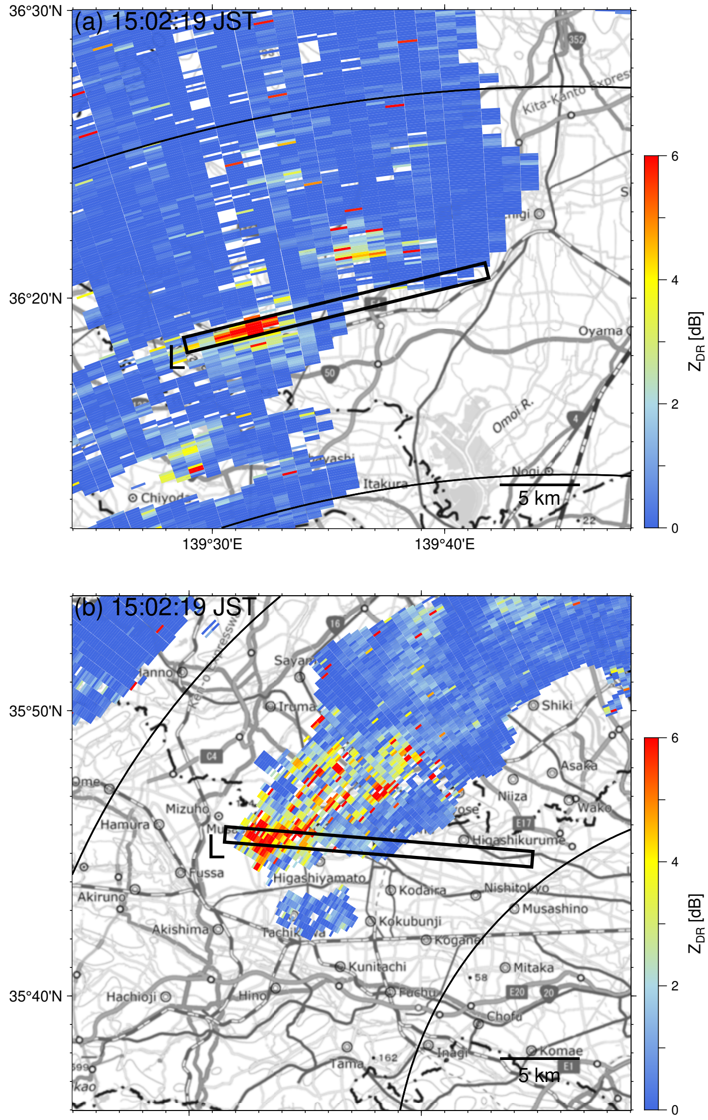

Fig. 9: PPI scan of Z_{DR} at 3.8° elevation angle performed by the Haneda radar at 15:02 JST on 11 July 2021. The base map was obtained from the GSI.
(a) A snapshot of Column A. Black arcs indicate 50-km and 100-km distances from the radar. Black rectangle (1×20 km) and letter "L" respectively denote the analyzed area and the starting point to count the horizontal distance in Figs. 10 and 11.
(b) A snapshot of Column B. Black arcs indicate 150-km and 200-km distances from the radar. Black rectangle (1×20 km) and letter "L" respectively denote the analyzed area and the starting point to count the horizontal distance in Fig. 13.

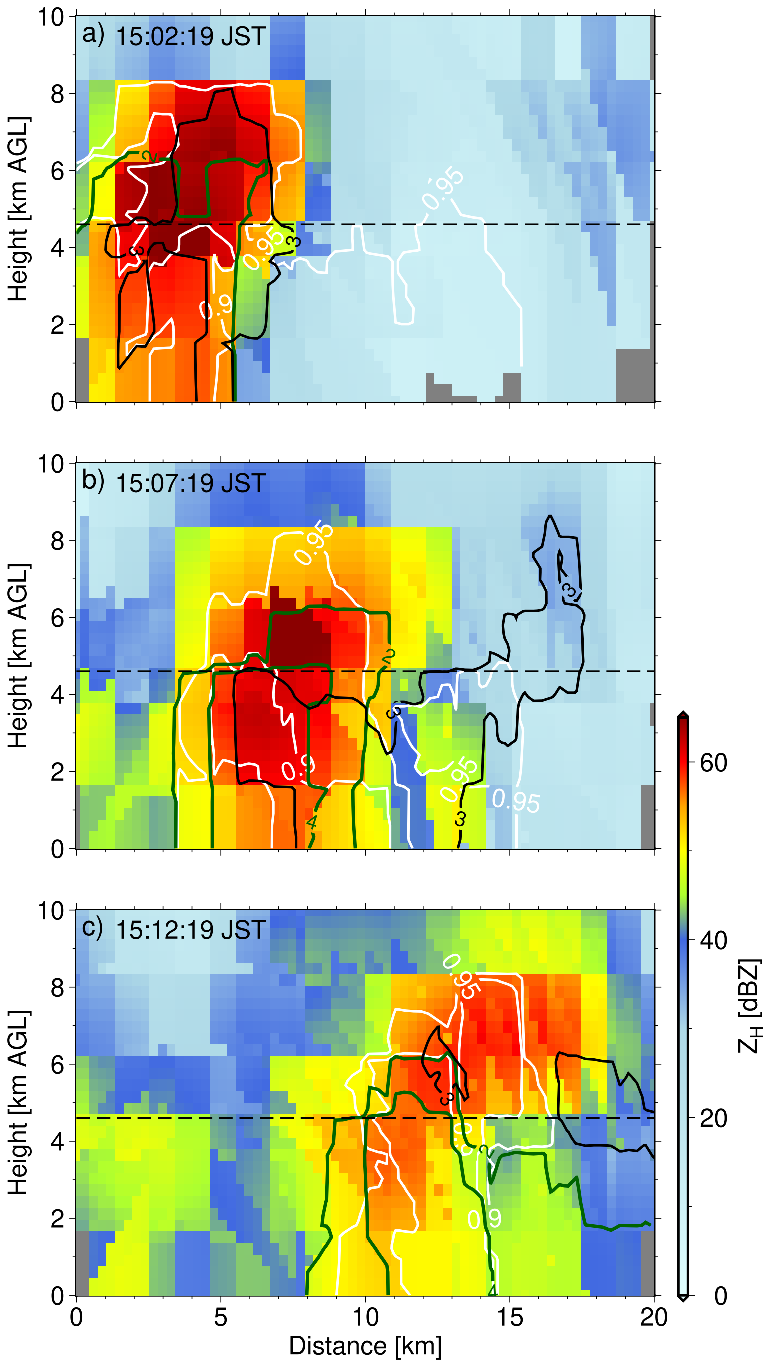

Fig. 10: Vertical distributions of Z_{H} overlaid with a Z_{DR} contour of 3 dB (solid black), K_{DP} contours of 2 and 4 deg/km (solid green), ρ_{HV} contours of 0.9 and 0.95 (solid white), the environmental 0 °C level of 4.6 km AGL (dashed black), and the observation time at 3.8° elevation angle in the upper left corner, representing the evolution of Column A. The horizontal axis represents the distance from the point denoted by the letter "L" in Fig. 9a. Note that Column A is the lower one with a height of 4.6 km AGL in (b).

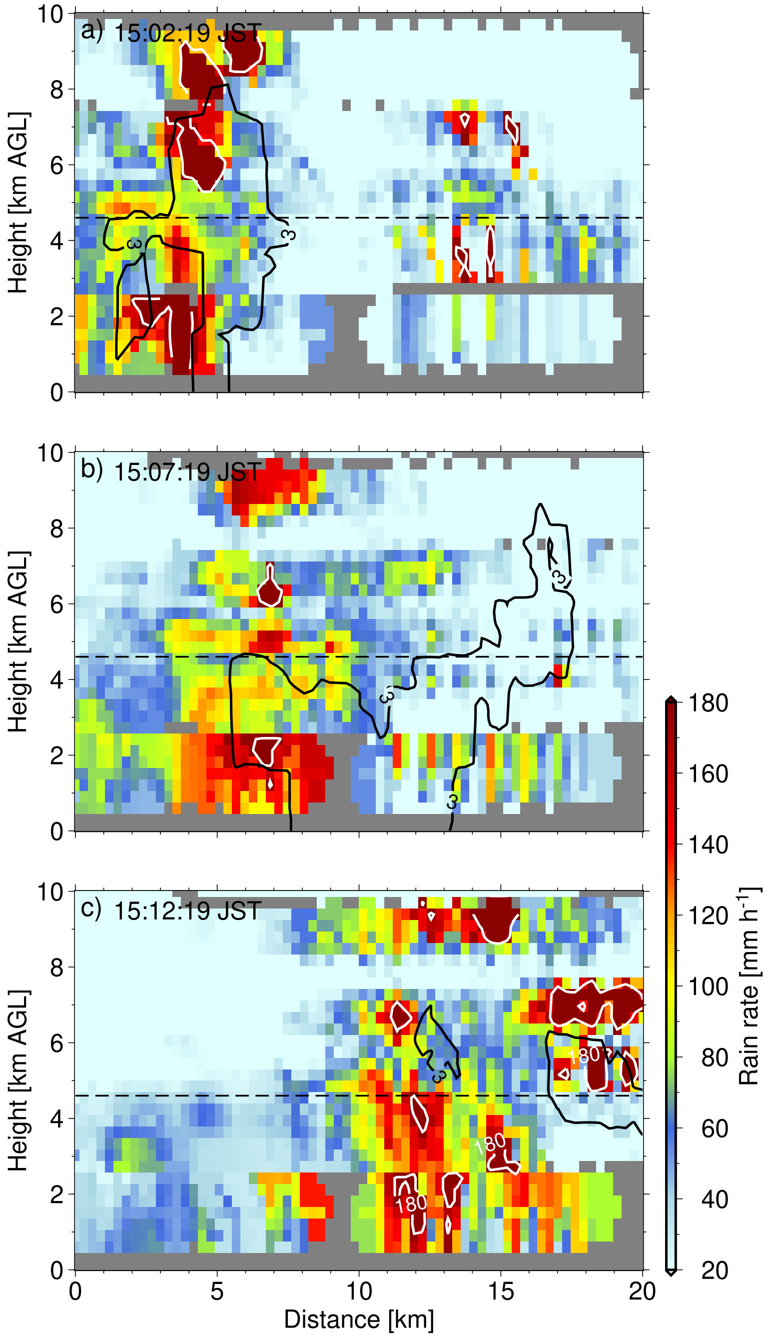

Fig. 11: As in Fig. 10, but the color scale represents the highest $R(K_{\mathrm{DP}}, Z_{\mathrm{H}})$ within a 1km-wide range of the area indicated in Fig. 9a, with the contour of 180 $\mathrm{mm\,h^{-1}}$ (solid white).

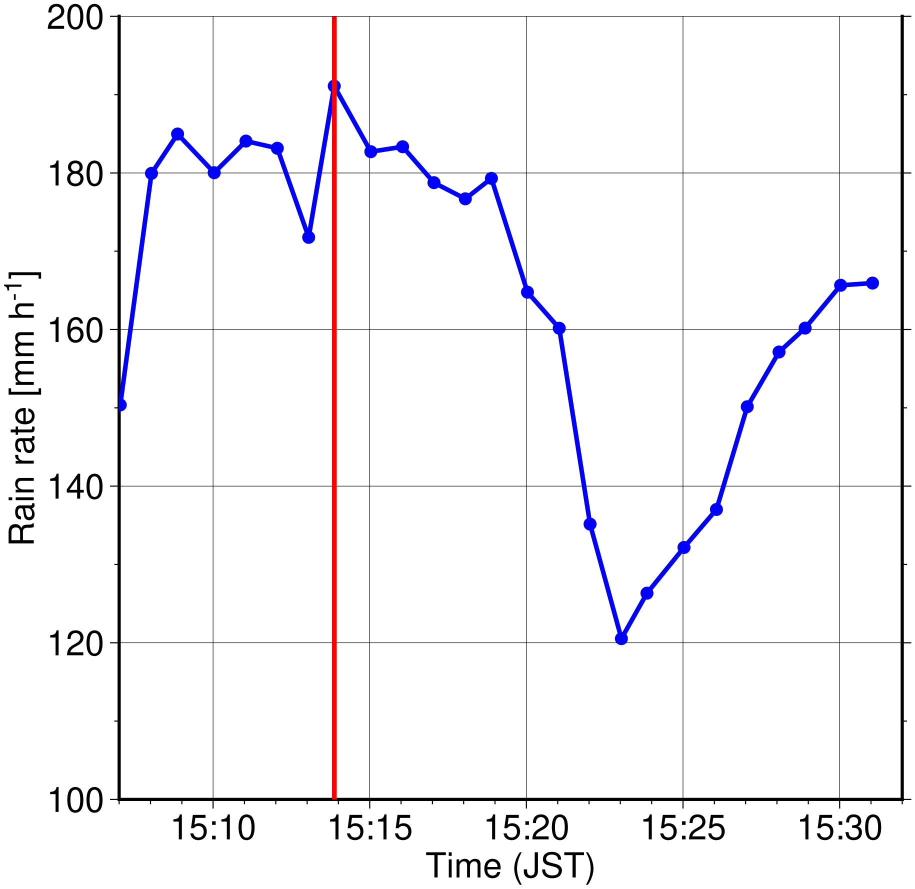

Fig. 12: Time series of the maximum rainfall rates within 5 - 30 minutes after the observation of the peak height of Column A observed at 15:02 JST at 0.7° elevation angle. The red line indicates the observation time of the momentary maximum rainfall rate.

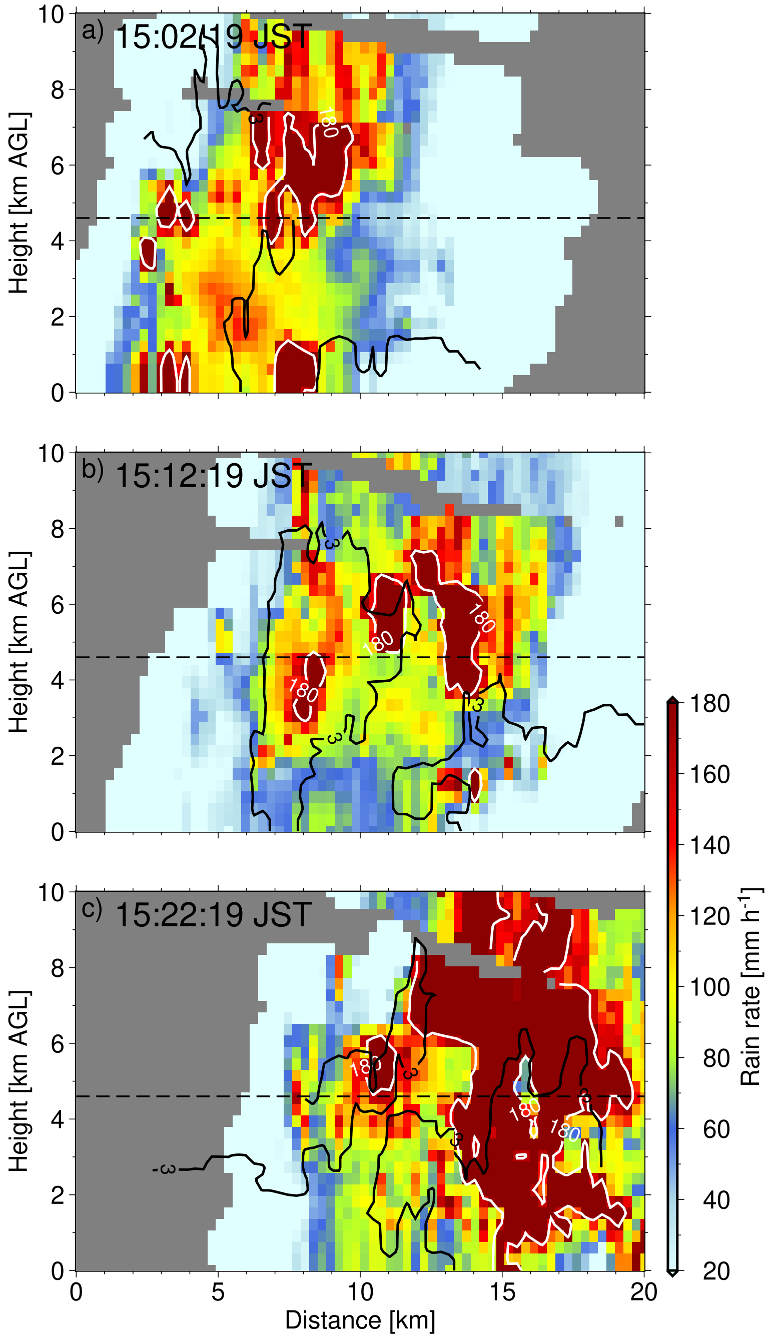

Fig. 13: As in Fig. 11, but the evolution of Column B is represented. The horizontal axis indicates the distance from the point denoted by the letter "L" in Fig. 9b.

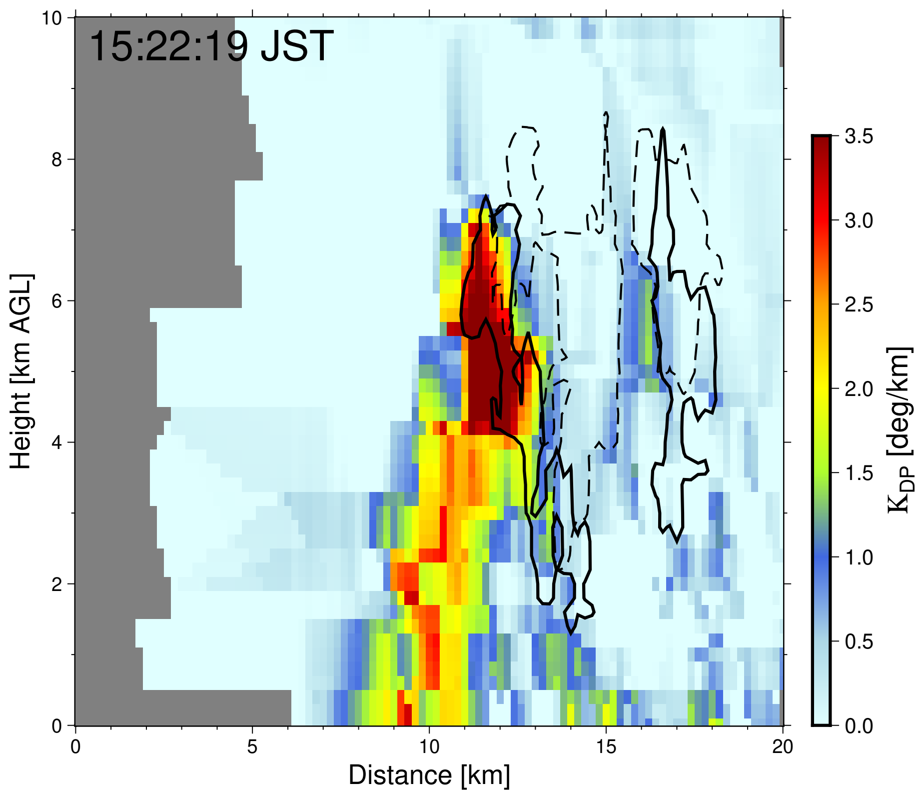

Fig. 14: Vertical distribution of K_{DP} calculated for Column B, overlaid with a ρ_{HV} contour of 0.86 (bold black), $R(K_{\mathrm{DP}}, Z_{\mathrm{H}})$ contour of 150 $\mathrm{mm\,h^{-1}}$ (dashed black), and the observation time in the upper left corner.

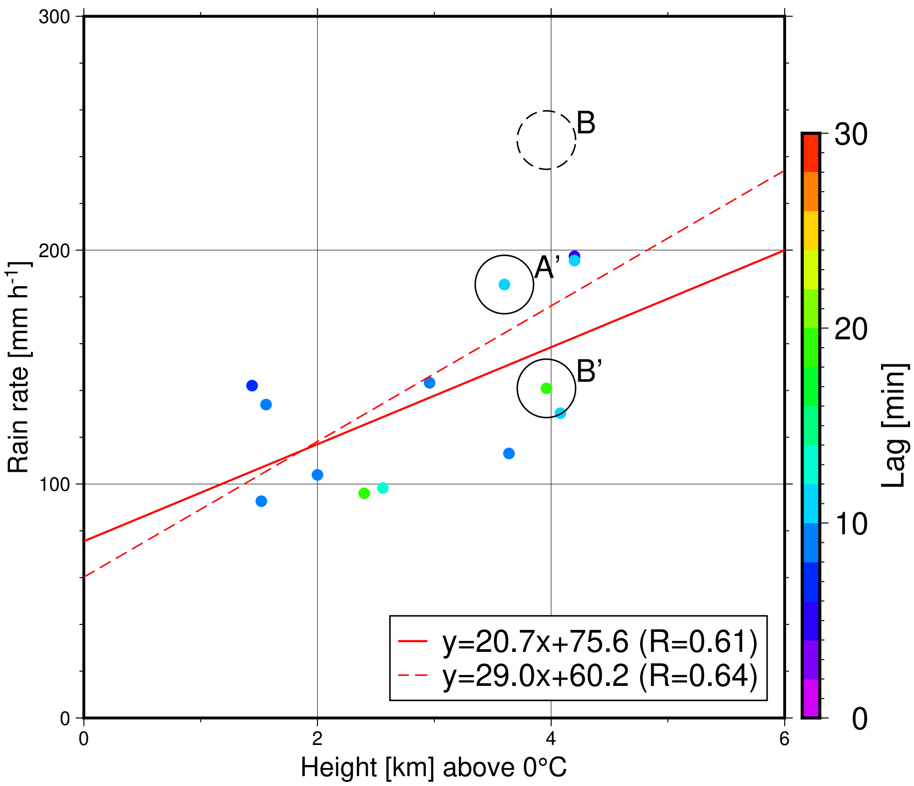

Fig. 15: As in Fig. 8, but the data are recalculated after eliminating those affected by hail. Solid black circles denote the data for Columns A′ and B′. For reference, the dashed black circle denotes the original data for Column B, and the dashed red line shows the linear regression before recalculation.

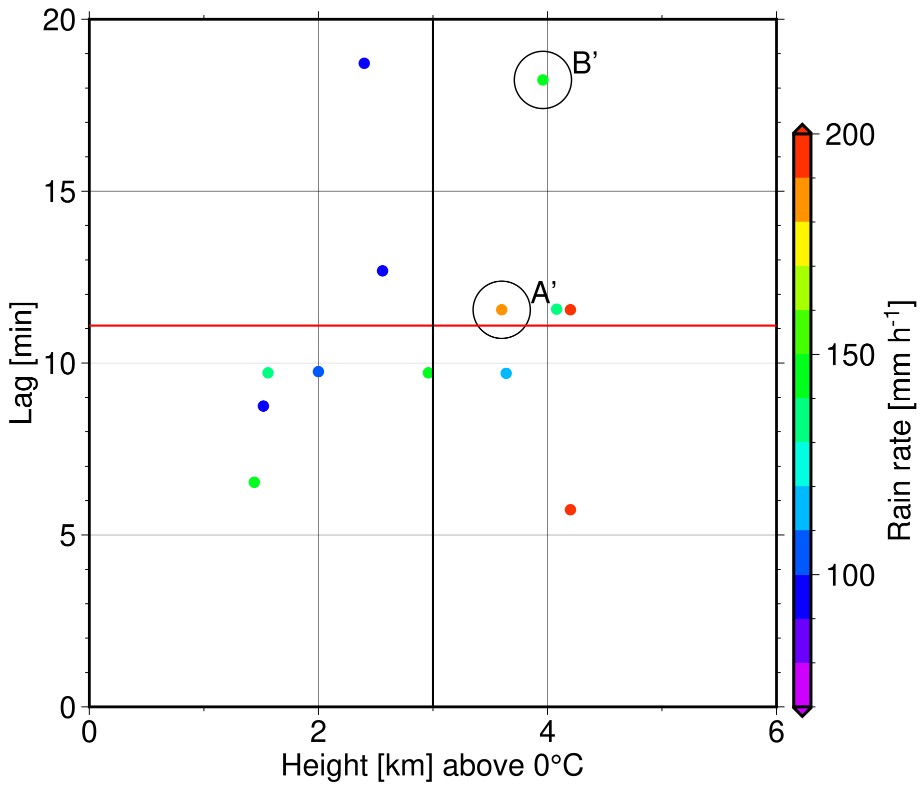

Fig. 16: Scatter plots of peak Z_{DR} column height above 0 °C level vs. lag time between peak column height and maximum rainfall rate observations, with the color scale representing maximum rainfall rates. Black and red lines respectively indicate 3 km height and mean lag time (11.1 min), and solid black circles denote the data for Columns A′ and B′.

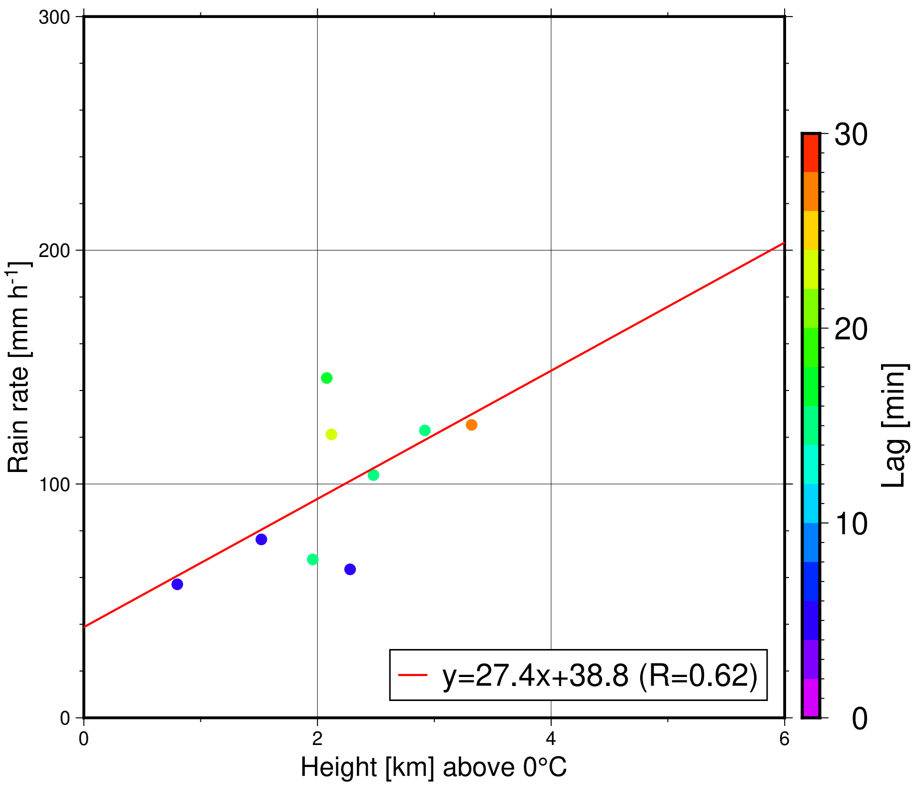

Fig. 17: As in Fig. 8, but the data were observed on 12 August 2020.

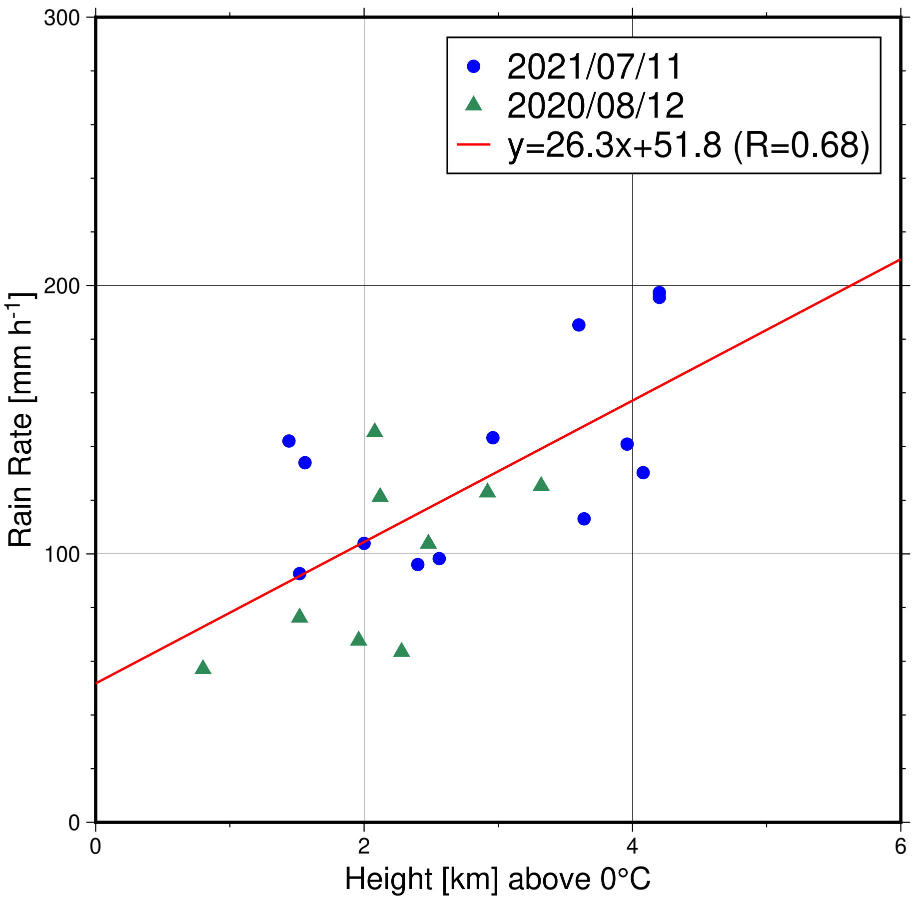

Fig. 18: Scatter plots of peak Z_{DR} column height above the 0 °C level vs. the maximum rainfall rate at low levels. Blue circular and green triangular dots respectively represent the data collected on 11 July 2021 and those on 12 August 2020. The red line shows the linear regression, and the regression equation and the correlation coefficient are shown in the upper right corner.

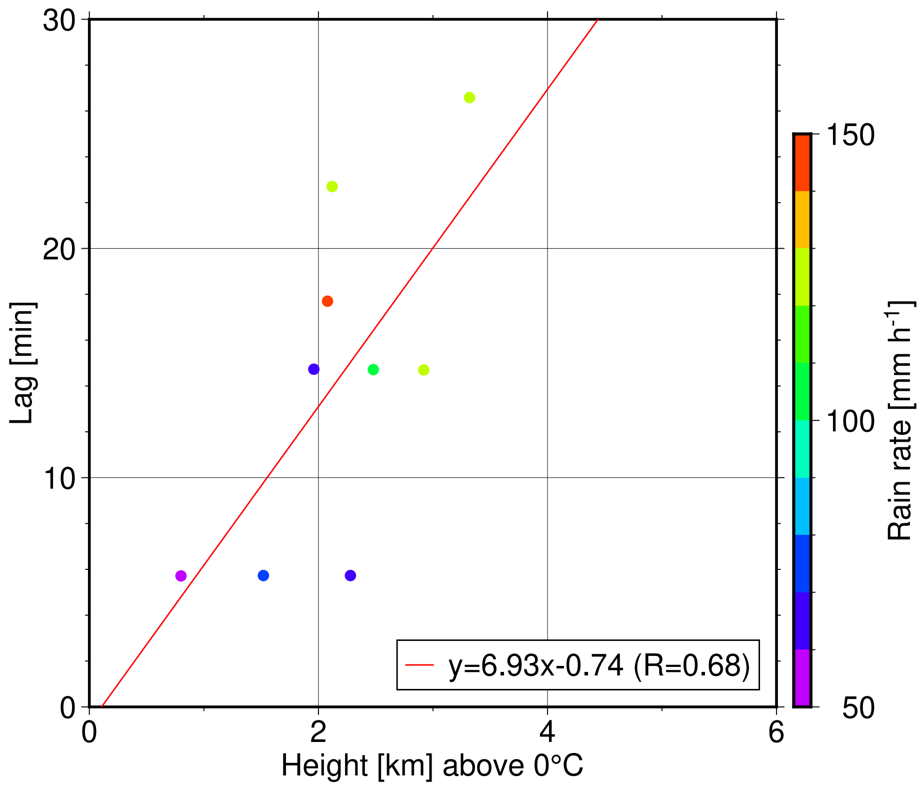

Fig. 19: As in Fig. 16, but the data were observed on 12 August 2020. The red line shows the linear regression, and the regression equation and the correlation coefficient are shown in the lower right corner.

List of Tables

Table 1: Operating characteristics of the Haneda radar

Frequency	5330 MHz
Peak power	5 kW
Pulse length	1 μs (short pulse) 64 μs (long pulse)
Antenna diameter	7.0 m
Antenna speed	4.2 rpm, 5.4 rpm, 7.0 rpm
Antenna gain (H and V)	> 49 dBi
Signal minimum	< -115 dBm
Cross-polar isolation	< -35 dB
Beam width	0.58° (horizontal) 0.59° (vertical)
Azimuthal resolution	0.7°
Transmitter	GaN HEMT
Range resolution	150 m
PRF	1040/832 Hz (0.7° $\leq$ Elv. $\leq$ 9.2°) 1365/1092 Hz (Elv. = 12.5°,17.0°,90°)